Journal of
Materials Chemistry C

Materials for optical, magnetic and electronic devices

This article can be cited before page numbers have been issued, to do this please use: G. Agnoloni, A. Carella, J. Staab, M. Arsentev, M. Lupi, S. Menichetti, C. Viglianisi, R. M. Young, F. Totti, M. R. Wasielewski, A. Privitera and R. Sessoli, *J. Mater. Chem. C*, 2026, DOI: 10.1039/D6TC01492E.

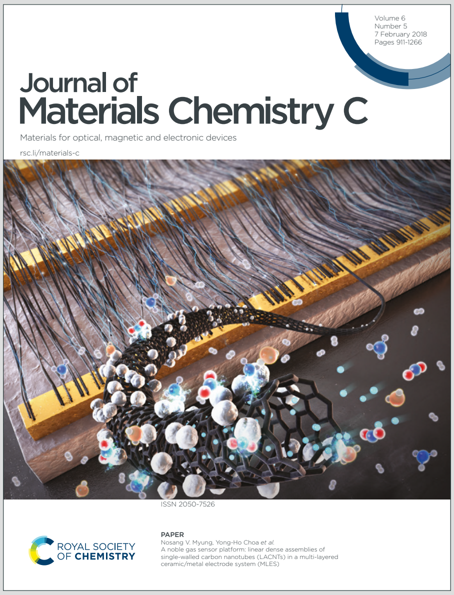

ROYAL SOCIETY
OF **CHEMISTRY**

rsc.li/materials-c

Spin-Selective Charge Transfer Pathways in Photoexcited Helicene-Perylenediimide Dyads

Received 00th January 20xx,
Accepted 00th January 20xx

DOI: 10.1039/x0xx00000x

Giulia Agnoloni,[a] Angelo Carella,[b,c] Jakob Staab,[a] Maksim Arsentev,[a] Michela Lupi,[a] Stefano Menichetti,[a] Caterina Viglianisi,[a] Ryan M. Young,[c] Federico Totti,[a] Michael R. Wasielewski,[c]* Alberto Privitera,[b,c]* and Roberta Sessoli[a]*

Spin-selective charge-transfer pathways in helicene-based dyads are relevant to applications ranging from energy conversion to quantum information science. Here, we report a series of molecular systems comprising a thiahelicene donor and a perylenediimide (PDI) acceptor connected by oligophenyl bridges of varying length. The influence of donor–acceptor distance and relative orientation on the photophysical and spin-selective properties is investigated using a combined approach based on DFT calculations, transient absorption, and time-resolved electron paramagnetic resonance spectroscopies. Particular attention is given to the role of the bridge in tuning exchange coupling within charge-transfer states and its impact on spin-selective recombination pathways to the PDI triplet state. Efficient formation of long-lived PDI triplets is observed and shown to sensitize singlet oxygen generation with high efficiencies. These results establish structure-property relationships governing spin-selective processes in helicene-based dyads.

Introduction

The investigation of spin-dependent pathways in donor–acceptor (D-A) molecules and materials has attracted increasing attention due to their relevance in a broad range of applications, including organic photovoltaics (OPVs),[1–5] photochemical processes.[6,7] and chiral-induced spin selectivity (CISS)–based technologies.[8–13] Within this framework, helicenes emerge as particularly attractive molecular building blocks.[14–22] Their intrinsic chirality, combined with strong π-conjugation and highly tunable electronic properties, makes them important platforms for applications spanning chiroptical materials to spin-dependent charge transport.[23–29] Among helicene derivatives, dithia-aza[4]helicenes (TAHEL) constitute a configurationally stable class of hetero[4]helicenes, owing to the presence of four long carbon-sulfur bonds.[17–22] These compounds are further distinguished by their ease of oxidation, which renders them excellent electron donors in donor–acceptor systems. Their radical cations can be readily generated via reversible oxidation with silver hexafluoroantimonate.[18]

The use of well-defined molecular architectures, in which the helicene donor is spatially separated from the acceptor through a precisely controlled molecular bridge, enables a systematic investigation of the key parameters governing charge-transfer processes and their associated spin selectivity.[30,31] Extensive studies have highlighted the critical role of the bridge in mediating the photoinduced electron transfer and charge recombination pathways.[32–35] In the context of emerging applications of D-A dyads in quantum information science, where the spin interactions must be precisely controlled, the use of rigid bridges is essential. In this regard, ethynylbenzene offers an optimal combination of conformational rigidity and efficient electronic communication between donor and acceptor moieties.

In our previous work, we investigated spin-correlated radical pairs (SCRPs) in dyads composed of a TAHEL donor and a perylenediimide (PDI) acceptor, connected by three ethynylbenzene units, forming a rigid, conjugated molecular wire.[36] Here, we extend this approach to a series of dyads featuring identical donor-acceptor units linked by systematically shortened ethynylbenzene bridges. The new donor-acceptor dyads have been studied using transient absorption (TA) and time-resolved electron paramagnetic resonance (TREPR) spectroscopies. The multi-step charge transfer (CT) process has been rationalized by ab initio calculations. Engineering the bridge enables precise control over both charge separation and charge recombination processes. In the shorter-bridge regime, the CT state lifetime becomes too short to be detected by TREPR spectroscopy, thereby shifting the focus toward triplet excited states and the mechanism of their formation. Spin-orbit charge-transfer intersystem crossing (SOCT-ISC) in electron donor-acceptor dyads is a promising approach to produce triplet states without the need for heavy atoms to increase spin-orbit coupling. The formation and fate of triplet excited states are central to optoelectronic applications and photochemistry, including processes such as singlet-oxygen sensitization in photodynamic therapy (PDT), and all investigate dyads exhibit significant $^1O_2$ generation efficiency.

Experimental Section

Synthesis. All chemicals were obtained from commercial suppliers and used as received without further purification. $Pd(PPh_3)Cl_2$, $Pd(PPh_3)_4$, and triflic anhydride were stored under nitrogen; triethylamine (TEA) and pyridine were freshly distilled over KOH before use. The acceptor unit was synthesized according to previously reported procedures.[37] The target donor–acceptor dyads were then obtained by reacting the acceptor unit with the donor–bridge intermediates. The two enantiomers of each donor-acceptor dyads were obtained by resolution through chiral HPLC (semipreparative CHIRALPACK® IG chiral stationary phase).

UV-VIS absorption and circular dichroism. UV-Vis absorption measurements were performed in toluene using a V-670 Jasco Spectrophotometer. Circular dichroism spectra were recorded in

---

[a] *Department of Chemistry "U. Schiff", University of Florence & UdR INSTM Firenze, 50019, Sesto Fiorentino, Italy.*

[b] *Department of Industrial Engineering, University of Florence & UdR INSTM Firenze, 50139, Firenze, Italy*

[c] *Department of Chemistry, Center for Molecular Quantum Transduction, and Institute for Quantum Information Research and Engineering, Northwestern University, 60208-3113, Evanston, IL (USA).*

View Article Online
DOI: 10.1039/D6TC01492E

DCM (HPLC grade) at a concentration of $2.4\text{x}10^{-5}$ M using the J-1500 circular dichroism spectrophotometer.

Cyclic Voltammetry. Electrochemical measurements were performed on a CH Instrument Model 622 electrochemical working station. Measurements were done in dichloromethane purged with argon, using a 0.1 M solution of n-butylammonium hexafluorophosphate ($TBAPF_6$), as supporting electrolyte, at a potential scan rate 100 mV s^{-1}. Potentials are referenced to the ferrocene/ferrocinium, Fc/Fc^+ redox couple. The counter electrode is a platinum wire, the working electrode is a 1.0 mm diameter glassy carbon electrode, and the reference electrode is a silver wire.

DFT calculations. Density functional (DFT) electronic structure calculations were carried out using the long-range corrected CAM-B3LYP[38] functional in conjunction with a polarizable continuum model to include environmental effects of the toluene solvent. A state-specific approach was applied to describe the ground and excited states, employing the spin-flip formulation of time-dependent DFT [39,40] to treat the locally excited *PDI state and the ΔSCF approach to treat the CT states, as implemented in the ORCA package.[40,41] The ΔSCF results were further used to simulate the CT state exchange coupling. All electronic structure calculations were based on structural models of the dyads replacing the PDI-based N-alkyl moiety with a N-CH3 group to reduce the computational complexity. Further methodological details are presented in Section S2.

TA spectroscopy. Femtosecond and nanosecond transient absorption (ns/fsTA) measurements were performed in toluene at room temperature using a commercial Ti:sapphire laser system (Tsunami oscillator/Spitfire amplifier, Spectra-Physics), as described previously.[42,43] Pump pulses at 530 nm were generated with a collinear optical parametric amplifier (TOPAS-Prime, Light Conversion, LLC) and attenuated to < 1 μJ/pulse. To suppress polarization-dependent dynamics, the pump pulses were depolarized using a DPU-25-A (Thorlabs Inc.) depolarizer. Samples (optical density 0.4-0.6 at 530 nm in a 2 mm cuvette) were degassed by repeated freeze-pump-thaw cycles to remove dissolved oxygen. TA spectra were corrected for group delay dispersion and scattered light using Surface Xplorer (Ultrafast Systems, LLC) prior to kinetic analysis. Global kinetic analysis was then performed to extract evolution-associated spectra and kinetic parameters, following procedures described previously.[44]

TREPR spectroscopy. X-band TREPR measurements were performed on a Bruker Elexsys E580 spectrometer equipped with a split-ring resonator (Bruker ER4118X-MS3). Sample temperature was controlled using an Oxford Instruments CF935 continuous-flow cryostat cooled with liquid nitrogen and an ITC503S temperature controller. The sample was photoexcited at 530 nm using 7 ns pulses from an optical parametric oscillator (Spectra-Physics BasiScan) pumped by the 355 nm output of a frequency-tripled Nd:YAG laser (Spectra-Physics Quanta-Ray Lab-150-10H) operating at 10 Hz. The laser light was delivered into the resonator via an optical fiber and collimator positioned outside the cryostat window, providing approximately 1 mJ per pulse with a beam diameter (FWHM) of ~5 mm. Following photoexcitation, transient magnetization time traces were recorded as a function of magnetic field using direct diode detection under continuous microwave irradiation (~0.2 mW). Data processing involved subtracting the background signal prior to the laser pulse for each kinetic trace (at a given magnetic field), followed by subtraction of the off-resonance signal for each spectrum (at any given time). Samples for TREPR measurements were dissolved in toluene (optical density ~1 at 530 nm) and sealed under vacuum after three freeze-pump-thaw cycles.

Singlet oxygen experiments. The experiments were carried out by comparison of the near-infrared photoluminescence (PL) intensity of singlet oxygen sensitized by dyads **1**, **1ph**, **2**, and **3**, PDI, and ZnTPP (used as a reference standard) in toluene (optical density ~1 for all samples), with a spectrofluorometer HORIBA Fluoromax Plus. PDI-based dyads were excited at 530 nm, whereas ZnTPP was excited at 550 nm.

Results and discussion

Synthesis, and UV-Vis absorption.

The D-A systems investigated, along with their general synthetic route, are presented in Scheme 1. Detailed procedures for their synthesis and full characterization are provided in the Supporting Information (SI). The bridging unit in **1** was 4-ethynyl aniline. For **2** and **3** the bridging units were prepared following the procedure reported in our previous work,[36] via a multistep process starting with the reaction of 4-iodophenol with trimethylsilylacetylene. In the case of **1ph**, the bridge unit was obtained through the reaction between 4'-((trimethylsilyl)ethynyl)-[1,1'-biphenyl]-4-amine and trimethylsilylacetylene. The donor-bridge intermediates were prepared by Sonogashira-Hagihara cross-coupling reaction (Scheme 1, a), in the presence of palladium acetate and triphenylphosphine. The reaction between the donor-bridge units and perylene monoimide leads to the formation of the final donor-acceptor dyads (Scheme 1, b).

View Article Online
DOI: 10.1039/D6TC01492E

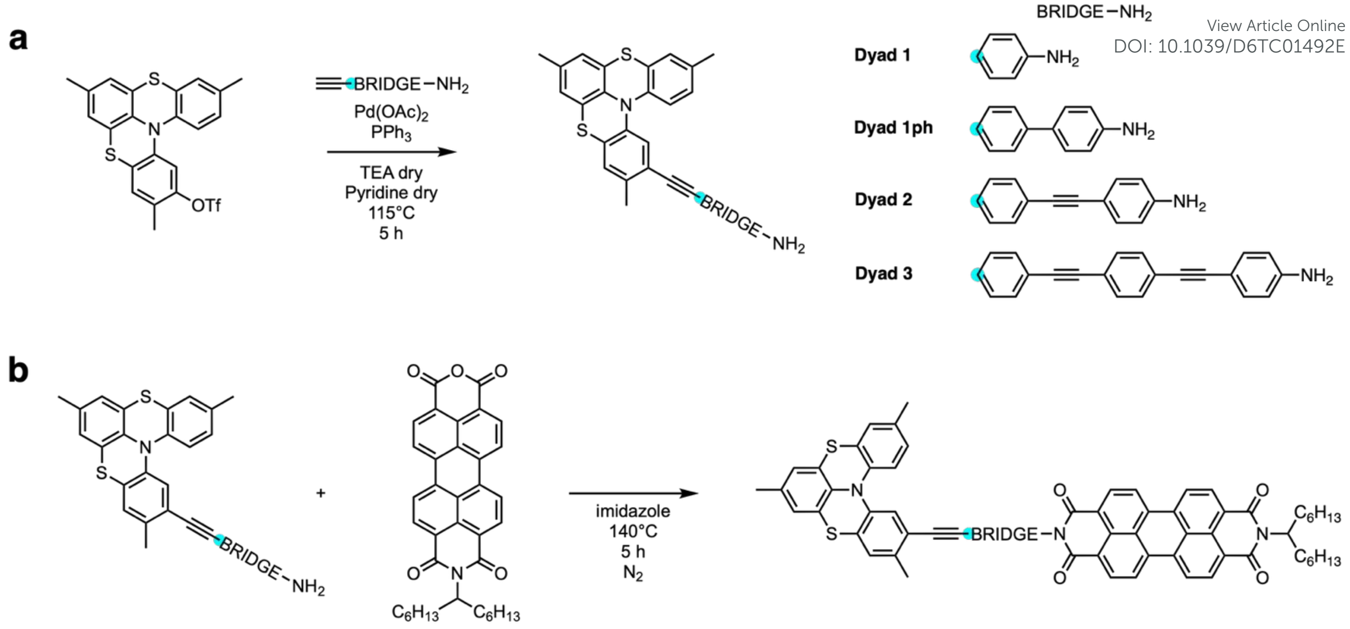

Scheme 1. (a) Synthesis of the donor-bridge units. (b) Synthesis of the final donor-acceptor dyads.

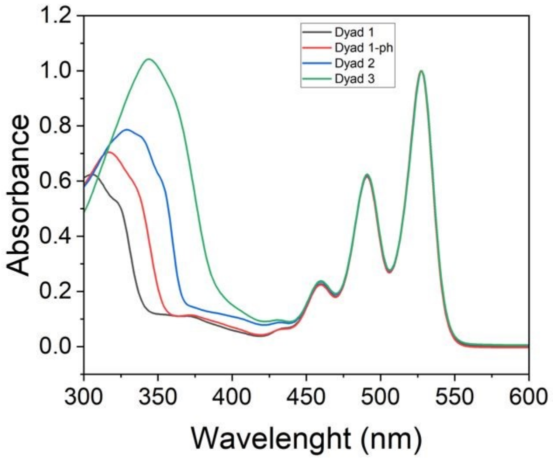

Figure 1. Normalized UV-VIS absorption spectra recorded in toluene at room temperature.

The ultraviolet-visible (UV-Vis) spectra of dyads **1**, **1ph**, **2**, and **3** have differing absorption maxima at wavelengths < 400 nm (Figure 1). The spectra are dominated by the PDI absorption bands at 527, 491, and 459 nm. The donor absorption region exhibits a red shift and increased intensity as the bridge length increases, likely due to enhanced conjugation between the donor and the bridge. More specifically, the donor absorption maximum is observed at 306 nm for **1**, 317 nm for **1ph**, 329 nm for **2**, and 344 nm for **3**.

Enantiomers of all dyads were separated by chiral chromatography and the enantiomeric excess determined from their chromatograms (Fig. S8-S15). The circular dichroism (CD) spectra were recorded in dichloromethane (HPLC grade) for all enantiomers and are shown in Fig. S16. The final donor–acceptor dyads are inherently chiral due to the presence of the chiral donor unit. Electronic communication between donor and acceptor is sufficient to enable electron transfer upon photoexcitation of the acceptor; however, it is not strong enough to induce chirality transfer to the acceptor. Accordingly, for all dyads no significant values for the dissymmetry factor are extracted from the CD spectral region dominated by the absorption of the PDI unit.[45]

Electrochemical studies.

To evaluate the Gibbs free energy changes associated with electron transfer and to determine the energy of the CT states in the D-A dyads, electrochemical measurements were carried out in CH_2Cl_2 (Figure 2). For all dyads there are two reversible reduction waves, which can be attributed to the PDI moiety, along with one reversible oxidation wave, assigned to the helicene moiety (Table 1). The single-electron oxidation corresponds to the removal of an electron from the donor-HOMO. The first of the two reduction processes consists of the addition of an electron into the acceptor LUMO, while the second reduction wave leads to the doubly reduced closed shell PDI^{2-} fragment, as suggested by the DFT calculations below. Notably, neither the oxidation potentials of the helicene donor nor the reduction potentials of the PDI acceptor are influenced by the nature of the bridge, as they remain essentially identical across all D-A dyads.

We used the Weller equation to estimate the free energy change, with respect to the ground state energy (ΔG_{IP}), associated with electron transfer from the donor to the acceptor to form the radical ion pair. To account for the different dielectric constants of dichloromethane (used for the electrochemical measurements) and toluene (used for the transient absorption experiments), Equation 1 was applied:[46]

$$\Delta G_{IP}=(E_{ox}\text{-}E_{red})\text{-}\left(\frac{{e_0}^2}{r_{DA}\varepsilon_S}\right)+\left({e_0}^2\left(\frac{1}{2r_D}+\frac{1}{2r_A}\right)\left(\frac{1}{\varepsilon_S}\text{-}\frac{1}{\varepsilon_{SP}}\right)\right)$$

Eqn. 1

where E_{ox} and E_{red} are the oxidation and reduction potentials of the donor and acceptor, respectively, measured in the

View Article Online
DOI: 10.1039/D6TC01492E

solvent used for the electrochemical experiments; ε_{SP} and ε_S are the static dielectric constants of dichloromethane and toluene, respectively;[47] ${e_0}^2$ is 14.4 eV·Å; r_{DA} is the center-to-center separation of the CT state; and r_D and r_A are the ionic radii of donor and acceptor, both calculated from the structures given by DFT calculations (see Table S1). The calculated values of ΔG_{IP} (Table 1) show a clear dependence on bridge length, increasing progressively from the shortest to the longest dyad. This trend is consistent with the reduced Coulombic stabilization of the CT state at larger donor-acceptor separations.

We have also calculated the Gibbs free energy change for the electron transfer process with respect to the PDI singlet excited state (ΔG_{ET}). The energy of the singlet excited state, ca. 2.33 eV, was determined as the cross point between the absorption and emission spectra of the molecules (see Figure S17). The value is in good agreement with the energy of the PDI excited singlet state previously reported,[48] and provides a negative (ΔG_{ET}) for all dyads (see Table 1).

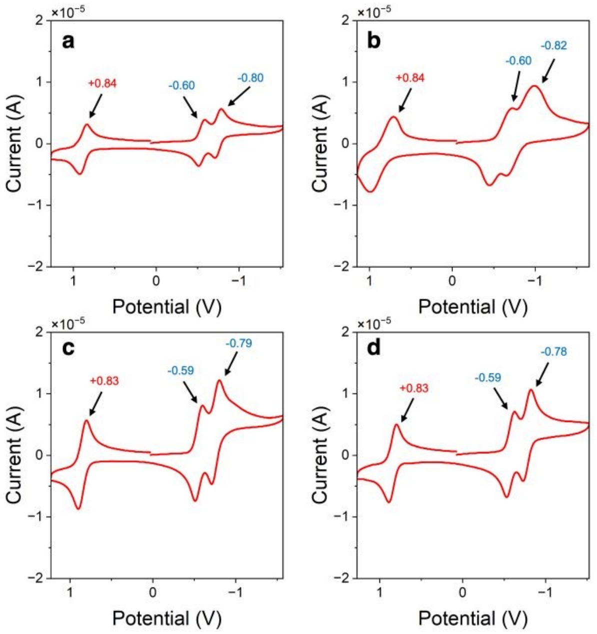

Figure 2. Cyclic voltammograms of (a) dyad **1**, (b) **1ph**, (c) **2**, (d) **3**. Measurements were performed in dichloromethane purged with argon, using a 0.1 M solution of n-butylammonium hexafluorophosphate (TBAPF$_6$), as supporting electrolyte, at a potential scan rate 100 mV s^{-1}. Potentials are referenced to the ferrocene/ferrocinium, Fc/Fc$^+$ redox couple.

Table 1. Electrochemical redox potentials of the compounds.

	E$_{ox}$ (V)	E$_{red1}$ (V)	E$_{red2}$ (V)	ΔG$_{IP}$ (eV)	ΔG$_{ET}$ (eV)
1	0.84	-0.60	-0.80	2.01	-0.32
1Ph	0.84	-0.60	-0.82	2.08	-0.25
2	0.83	-0.59	-0.79	2.10	-0.22
3	0.83	-0.59	-0.78	2.15	-0.18

DFT calculations: Molecular structures and energy levels.

DFT electronic structure calculations were employed to gain further insight into the photophysical and electrochemical properties as well as the CT dynamics (see section S3 of SI for methodological details). As shown in Figure 3b, the closed-shell ground state exhibits a pair of π-orbitals as HOMO and LUMO, which are strongly localized on the opposite TAHEL and PDI moieties of the dyad, respectively. Crucially, the conjugation of the π-system is broken at the PDI-bridge interface, partitioning the dyad into largely electronically isolated PDI and TAHEL/bridge fragments. Within this picture, the HOMO-LUMO transition represents the lowest-lying CT state. In contrast, the lowest-lying locally excited PDI and TAHEL states are well described by promoting an electron from the PDI HOMO orbital to the LUMO and by promoting an electron from the TAHEL/bridge-based HOMO orbital to the TAHEL/bridge-based LUMO, respectively. Furthermore, the single-electron oxidation and reduction processes are represented by the removal of an electron from the TAHEL-based HOMO and by the addition of an electron into the PDI-based LUMO, respectively. Based on the energetics of the frontier orbitals (see Figure S20), we conclude that the second reduction consistently yields the doubly reduced closed shell PDI^{2-} fragment. We demonstrated this explicitly employing ab initio calculation of the singly and doubly reduced dyad **1** and isolated PDI species (see Section S3 of SI). The LUMO remains fully localized on the PDI unit throughout the series, indicating that the reduction process is PDI-centered.

Table 2. Computed Gibbs free energies, exchange coupling constant *J* (in the $JS_D \cdot S_A$ convention) and magnitude of the dipole moment in the CT$_1$ and CT$_2$ states as well as D-A distance r_{DA} determined as the distance between the TAHEL nitrogen and the geometrical center of the PDI system.

	ΔG$_{IP}$ (ev)	J_{CT1} (cm^{-1})	J_{CT2} (cm^{-1})	$|\mu|_{CT1}$ (Å e)	$|\mu|_{CT2}$ (Å e)
1	1.82	+0.045	-8.5	15.55	12.39
1ph	1.91	-0.0012	-3.6	19.82	15.31
2	1.94	-0.0012	-5.4	22.31	15.83
3	2.03	-0.00058	-4.6	29.08	16.63

As shown in Figure 3b, after photo-excitation, electron transfer from the ^{1}*PDI state is likely initiated via the partially charge-separated CT$_2$ state owing to its favorable energetic alignment and then proceeds to the fully charge-separated CT$_1$ state. The donor magnetic orbital in CT$_1$ exhibits a higher degree of localization on the TAHEL fragment (see Figure 3a, and Figure S20), thus leading to a larger magnitude of the dipole moment μ, and weaker exchange coupling *J* (see Table 2). Here, the exchange interaction between the two photogenerated radical centers S$_D$ and S$_A$ is described by the isotropic spin Hamiltonian H_{ex}=$JS_D \cdot S_A$. Among the dyads studied, the dipole moment increases (**1** < **1ph** < **2** < **3**), while the magnitude of the exchange coupling constant decreases (**1** > **1ph** ≈ **2** > **3**), which is consistent with D-A separation and degree of π-conjugation of

View Article Online
DOI: 10.1039/D6TC01402E

the bridge. A similar reduction of *J* as in **1** → **2** is observed for **1** → **1ph**, suggesting that electronic π-system disruption by the additional torsion between the two phenyl rings is equivalent to spatial bridge elongation. In case of the CT_2 states, stronger interactions are obtained with a less pronounced variation along the series because the magnetic orbital localized on the helicene moiety extends evenly over the full length of the π-system of the bridge.

Two further notable trends are observed regarding the excited states across the series of dyads: (i) The vertical excitation and Gibbs free energy of the fully charge-separated state CT_1 increases with increasing bridge length, while (ii) the excitation energy of the higher lying states CT_n (n>1) decreases. In line with the results obtained from the Weller equation, the former is a direct result of Coulomb's law (attenuated by the solvent polarization) in conjunction with strong localization of the electron (and hole) on A (and D), i.e. the electrostatic energy is inversely proportional to the separation of the charge governed by the D-A distance. The latter observation again reflects the growing size of the extended π-system of the bridge, leading to an increasing stabilization of the CT_n (n>1) excitation, which features significant electron delocalization onto the bridge.

An alternative set of DFT calculations employing the methodology from ref. [36], which recovers all qualitative results discussed here, is presented in section S3 of SI.

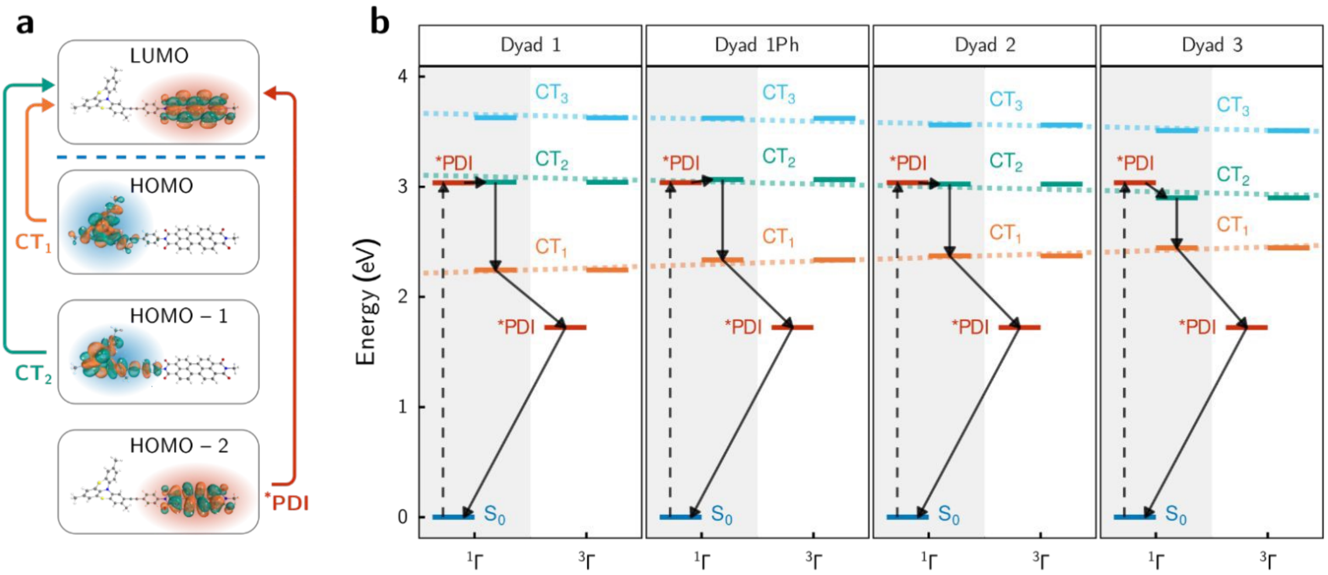

Figure 3. (**a**) Orbital excitations characterizing relevant excited states participating in the photophysical pathway. (**b**) The corresponding DFT ground and vertically excited singlet ($^1\Gamma$) and triplet ($^3\Gamma$) state energy levels. Arrows depict the plausible pathway of photo-excitation, (partial and full) charge-separation, intersystem crossing, and final charge recombination. These results correspond to a computational protocol employing the spin-flip time-dependent DFT approach for the locally excited *PDI state, while the ΔSCF method is used to describe the CT states. CT states are labelled by increasing energy (CT_1 lowest, CT_2 higher, etc.).

Transient Absorption Spectroscopy.

The charge transfer and recombination dynamics of the four dyads in toluene at room temperature were measured using a 120 fs pump pulse and probing from 300 fs to 300 µs over 390–1500 nm wavelength range. Figure 4a shows the TA spectra for **1** as a representative system at key delays after the laser flash, while data for the other dyads are included in Figures S22-S24a of the Supporting Information. Fitted kinetic traces, evolution-associated spectra (EAS), and model population dynamics from global fitting are provided in Figures 4b-d (**1**) and S22-S24b-d (**1ph, 2, 3**), with the corresponding parameters summarized in Table S3. The TA global fitting analysis, supported by DFT-calculated energy states, outlines the photophysical picture shown in Figure 4e.

Upon PDI photoexcitation at 527 nm, **1** displays the characteristic signals of the PDI excited single state (^{1*}PDI),[49,50] including ground-state bleaching (GSB) from 400 to 550 nm, stimulated emission (SE) centered at 580 nm, and excited-state absorption (ESA) centered at ~ 700 nm. Within 8.6 ps, the SE vanishes, and an ESA peak at 960 nm, characteristic of the PDI radical anion ($PDI^{-\bullet}$), confirms the formation of a CT state.[49,50] This state is accompanied by broad NIR absorption between 1100–1500 nm, attributed to the TAHEL cation.[21] From the global fitting analysis, a subsequent transition with a rate constant of 1.2 ns occurs. As shown in Figure 4c, the EAS for states B and C are similar, differing only in amplitude and kinetics. This suggests that both states correspond to a similar electronic state - the CT state - and that the transition reflects only minimal wavefunction rearrangement. The two EAS are associated with the CT_1 and CT_2 states: an initial hole transfer generates CT_2, followed by hole relaxation to CT_1 on a ~1 ns timescale. At later times (~9.3 ns), the signal from the relaxed CT state decreases, leading to the emergence of a spectrum corresponding to the low-lying excited state of PDI (^{3*}PDI) generated by charge recombination. This spectrum features ESA between 400 and 600 nm, which is superimposed on the GSB of the PDI.

View Article Online
DOI: 10.1039/D5TC01492E

The TA analysis on the series suggests a similar photophysical pathway for the other dyads, with time constants listed in Table 3. For the analysis, a sequential model was employed, which provides a well-established qualitative description of the photophysical landscape of D–A dyads.[11–13,36,51] The first process, A→B, corresponding to hole transfer from ^{1*}PDI to CT_2, depends on the bridge length, indicating that the through-bond electronic coupling between TAHEL and PDI decreases as their distance increases.[52] Based on PDI fluorescence lifetime (~3.7 ns),[48,53] we estimate that the hole transfer quantum yields are 99.7% in **1**, 99.2% in **1ph**, 98.5% in **2** and 90.5% in **3**. The second step, B → C, occurs on the order of ~1 nanosecond across all dyads with minimal bridge dependence, suggesting it corresponds to hole relaxation ($CT_2 \rightarrow CT_1$), which is only slightly influenced by bridge length. The third step, C → D, corresponds to the recombination of the CT state to ^{3*}PDI. This process generally slows down with increasing bridge length, mirroring the trend observed for the forward charge-transfer step. Notably, **3** deviates from this trend, showing a faster recombination to the triplet state than **2**, suggesting a change in the dominant recombination pathway.

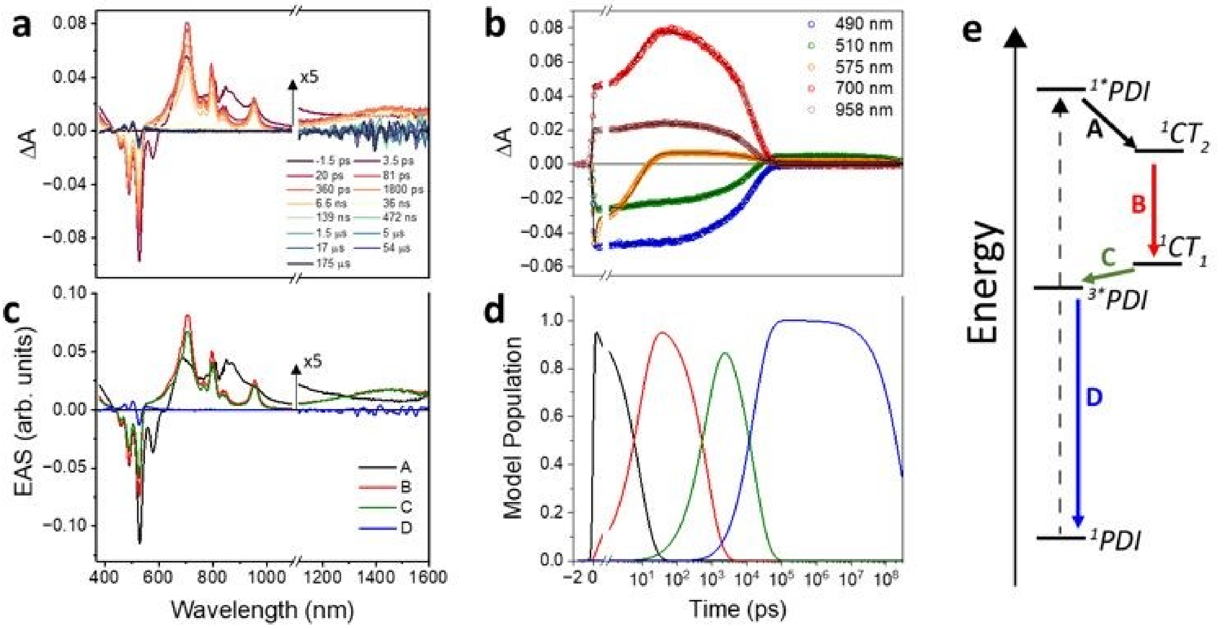

Figure 4. (a) Room-temperature fs/nsTA spectra of **1** in toluene excited at 527 nm and recorded at selected delay times. (b) Selected wavelength kinetic fits, (c) evolution-associated spectra (EAS) and (d) population dynamics obtained by globally fitting the fs/nsTA data. The mechanism assumed to fit the data is A → B → C → D → ground state, where state A represents the singlet excited state of PDI, B is the CT_2 state, C is the CT_1 state, and D is the excited triplet state of PDI. (e) Qualitative Jablonski diagram illustrating hole transfer and charge recombination, with photophysical steps labelled according to EAS and model populations based on energy levels derived from TD-DFT calculations.

Table 3. Best values obtained from the kinetic fits of the TA spectra in Figures 4 and SI1-3.

	A→B (ps)	B→C (ns)	C→D (ns)
1	8.4 ± 0.3	0.8 ± 0.1	16.3 ± 0.1
1Ph	29.9 ± 0.3	1.0 ± 0.1	99.8 ± 0.1
2	54.1 ± 0.3	1.1 ± 0.1	227 ± 1
3	350 ± 5	1.6 ± 0.3	156 ± 1

To gain further insight into the distance dependence of the charge-transfer and charge-recombination processes in the dyads, the corresponding rate constants were plotted as a function of the D-A separation (Figures 5a,b). For all dyads, the charge-separation rate constants (k_{CT}) decrease exponentially with increasing D-A distance according to $k_{CT}(r)=k_0\exp[-\beta(r-r_0)]$, where k_0 is the rate constant at the contact distance r_0. A decay constant $\beta \approx 0.11 \pm 0.01$ Å^{-1} is obtained, indicating a weak attenuation of electronic coupling with distance. This behavior is consistent with a superexchange-mediated hole-transfer mechanism from ^{1*}PDI to the TAHEL donor. A similar exponential distance dependence was reported previously for phenothiazine-bridge-PDI dyads employing p-phenylene oligomer bridges.[49] In the present case, the slightly smaller β value reflects a more efficient electronic delocalization along the π-conjugated bridge, likely promoted by the presence of the triple bond between adjacent phenyl units.

Similarly, for dyads **1**, **1ph**, and **2**, the charge-recombination rate constants (k_{CR}) follow an exponential decay with distance, yielding $\beta \approx 0.20 \pm 0.02$ Å^{-1}. In contrast, **3** deviates from this trend, displaying an increase in k_{CR} with increasing bridge length. Such behavior has been observed previously in related systems[49] and was motivated with a change in the dominant recombination mechanism upon bridge extension. Specifically, a crossover from superexchange-mediated recombination to a thermally activated hopping process was proposed for phenyl-

View Article Online
DOI: 10.1039/D6TC01492E

bridged dyads. Although our calculations indicate that CT$_2$ remains thermally inaccessible from CT$_1$ for all dyads, a clear trend emerges in which the CT$_2$-CT$_1$ energy gap decreases with increasing bridge length (see the eye-guide broken line in Figure 3b). This evolution may suggest that a similar mechanism to that proposed in ref.[49] could account for the behavior observed here.

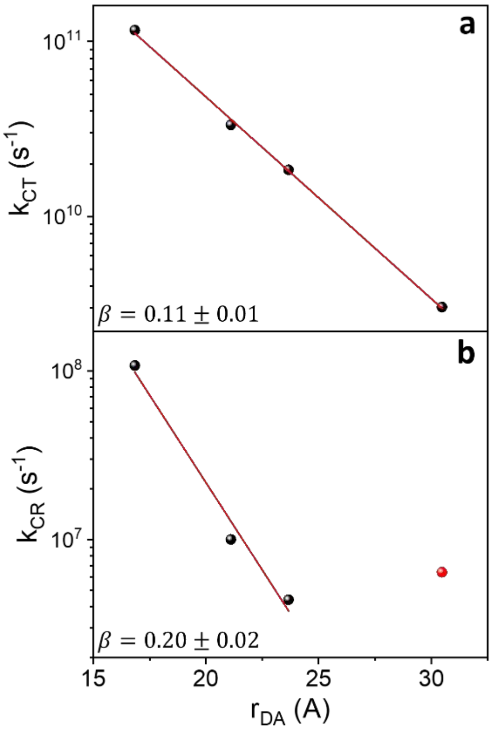

Figure 5. (a) Semi-logarithmic plot of the charge-transfer rate constant (k_{CT}) as a function of the D-A distance (r_{DA}). A linear fit to the data points yields $R^2 = 0.999$, $\beta = 0.11 \pm 0.01$ Å^{-1}, and $k_0 = (9.7 \pm 0.1) \times 10^{12}$ s^{-1}. (b) Logarithmic plot of the charge-recombination rate constant (k_{CR}) versus the D-A distance (r_{DA}). A linear fit to the data points (excluding dyad **3**) gives $R^2 = 0.983$, $\beta = 0.20 \pm 0.02$ Å^{-1}, and $k_0 = (3.0 \pm 0.1) \times 10^{11}$ s^{-1}. Error bars are smaller than the symbol size and not visible in the semi-logarithmic plot.

TREPR spectroscopy.

Overall, the TA characterization reveals a similar photophysical pathway across all dyads, with differences primarily in bridge-dependent kinetics. We next examine the spin-selectivity of the charge-transfer pathways using continuous-wave time-resolved electron paramagnetic resonance (TREPR) spectroscopy. In contrast to TA, TREPR provides direct information on spin interactions and spin-dependent photophysical pathways, offering a complementary view of the bridge role in spin dynamics. Figure 6a-d show the TREPR spectra (black lines) of all dyads in toluene solution, recorded at 85 K after photoexcitation at 527 nm. All spectra show a broad signal between 290 mT and 390 mT, reminiscent of what reported for PDI-centered triplet states.[47,54–57] Best-fit simulations (red lines) assuming S=1 are included, with parameters listed in Table S2. From the best-fit simulations, the zero-field splitting values *D* ~ 1300 MHz and *E* ~ -120 MHz are obtained, which are assigned to the PDI triplet excited state.[54,58] The principal axes of the ZFS tensor are defined such that the *Z*-axis is perpendicular to the molecular plane, the *Y*-axis lies along the N-N direction, and the *X*-axis is orthogonal to both. Interestingly, direct intersystem crossing via SO-ISC is negligible for ^{1*}PDI → ^{3*}PDI since the fluorescence quantum yield of PDI is approximately unity.[48,59] This suggests that radical pair formation plays a key role in driving the ISC in our dyads. In this context, the electron spin polarization (ESP) offers valuable insight.

The ESP phase pattern varies across the dyads' spectra, indicating different triplet generation pathways. For **1**, the ESP pattern is *eaeaea*, where *e* represents emission and *a* indicates enhanced absorption. This ESP pattern is characteristic of the spin-orbit charge-transfer (SOCT) ISC mechanism, which has been extensively documented in the literature.[54,58,60–68] This mechanism is initiated by charge transfer, leading to the formation of the singlet radical pair ^{1}(D$^{+\bullet}$-B-A$^{-\bullet}$). It is observed when the exchange interaction between the two radicals exceeds both their electronic Zeeman energy difference and the hyperfine interactions within each radical. From the singlet radical pair, rapid ISC can occur through charge recombination and generate D-B-^{3*}A. This process can occur when the orientations of the D and A SOMOs allow a significant change in orbital angular momentum during recombination, compensating for the electron spin flip. This condition is met in the TAHEL–PDI dyads, where calculated geometries show that the TAHEL$^{+\bullet}$ and PDI$^{-\bullet}$ SOMOs are nearly perpendicular (**1**-**3**) or strongly tilted (38.7°, **1ph**). In SOCT-ISC, the three zero-field sublevels T$_X$, T$_Y$, T$_Z$ of D-B-^{3*}A are selectively populated. In dyad **1**, the T$_Y$ level is preferentially populated, in agreement with previous reports,[54] and the six EPR transitions from low to high field exhibit an *eaeaea* polarization pattern, as represented in Figure 6e.

For **1ph** and **2**, best-fit spectral simulations reveal two ESP contributions (Table S2). The first is *eaeaea,* attributed to the SOCT-ISC, while the second is *aeeaae*, characteristic of radical pair intersystem crossing (RP-ISC).[58,59] This ISC mechanism also involves the formation of a radical pair, but in this case, the exchange interaction is smaller than the difference in electron Zeeman energy and the hyperfine interaction. After charge transfer, the initial singlet radical pair ^{1}(D$^{+\bullet}$-B-A$^{-\bullet}$) undergoes radical pair ISC (RP-ISC), driven by hyperfine coupling and the electronic Zeeman energy difference, to produce a triplet radical pair ^{3}(D$^{+\bullet}$-B-A$^{-\bullet}$).[10,31] The subsequent charge recombination is spin-selective: the singlet radical pair recombines to the singlet ground state, whereas the triplet radical pair recombines to form ^{3*}PDI with a distinct ESP pattern. RP-ISC operates directly on the high-field triplet sublevels of the radical pair, preserving spin polarization upon recombination. In dyads **1ph** and **2**, recombination occurs mainly on the T$_0$ localized triplet sublevel, and the resulting ESP shows an *aeeaae* pattern (Figure 6e), a clear signature of the RP-ISC mechanism within D$^{+\bullet}$-B-A$^{-\bullet}$.

Dyad **3** exhibits only a single ESP contribution - the *aeeaae* pattern - indicating the exclusive presence of the RP-ISC mechanism. Interestingly, a narrower signal appears at the center of the spectrum (Figure S25), with distinct features of a spin-correlated radical pair (SCRP).[10,12,13,31] The SCRP signal

View Article Online
DOI: 10.1039/D5TC01492E

completely disappears in ~ 1 µs, leaving only the RP-ISC triplet spectrum. This signal has been discussed in detail in our previous publication and is not further considered here.[36]

Both SOCT-ISC and RP-ISC depend on the relative orientation of the orbitals involved in charge transfer and on the magnitude of the exchange coupling in the CT_1 state.[49,50] DFT calculations indicate a decrease in exchange coupling between the donor radical cation and acceptor radical anion from **1** to **3**. This trend is fully reflected in the experimental TREPR observations, where SOCT-ISC dominates in dyad **1**, both mechanisms contribute in dyads **1ph** and **2**, and RP-ISC dominates in **3**. Even if an accurate DFT estimation of *J* is challenged by their small values,[69,70] the computed *J* for **3** approaches the difference in Zeeman energy between $D^{+\bullet}$ and $A^{-\bullet}$ radicals, estimated in ~ $3x10^{-4}$ cm^{-1} at X-band by assuming that the thiahelicene radical has $g_{iso} = 2.0043$, and the donor hyperfine interaction ($A_{iso}(N)$ ~ $6x10^{-4}$ cm^{-1}).[36] The coexistence of both mechanisms in **1ph** and **2** is not uncommon and has been previously reported in other PDI-based dyads.[49,50]

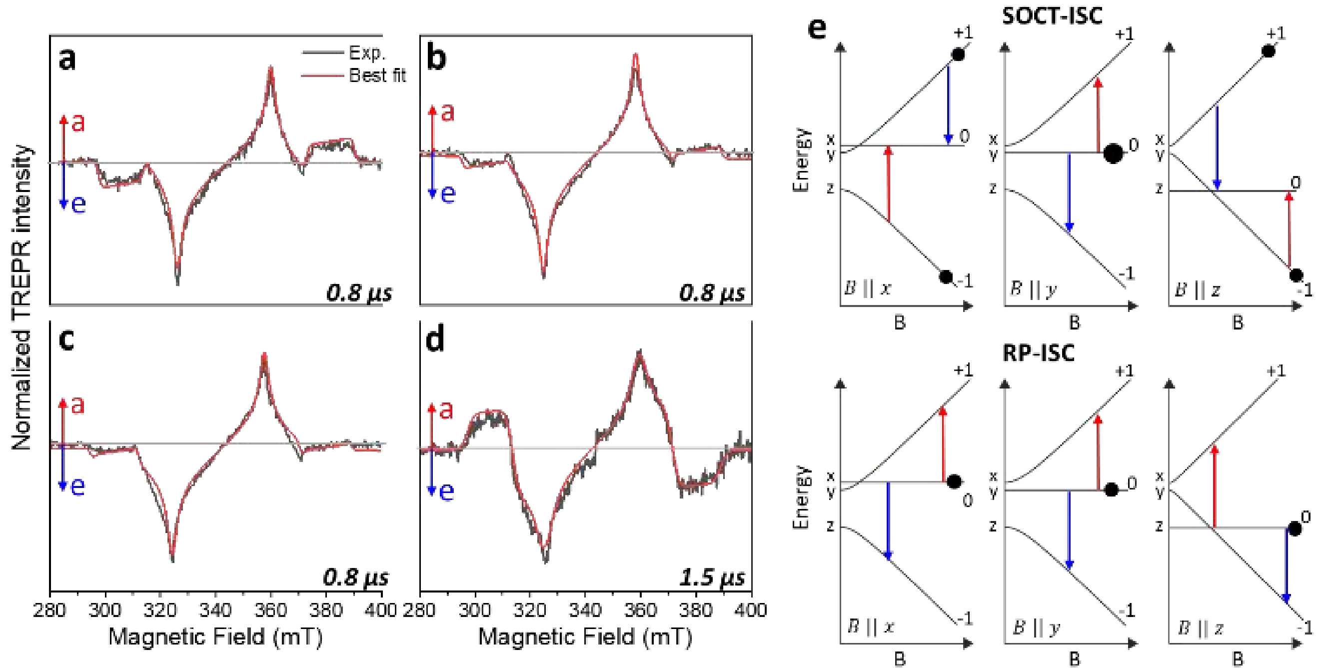

Figure 6. Experimental TREPR spectra (black traces) of (a) dyad **1**, (b) dyad **1ph**, (c) dyad **2**, (d) dyad **3** in toluene at 85 K, taken at representative times after the laser pulse (integrated time window = 100 ns). For dyad **3**, the spectrum is shown at a delay of 1.5 µs after the laser pulse, when the radical pair signal has decayed (see Figure S25). Simulations of the spectra (red traces) used the parameters given in Table S2. Arrows legend: a = enhanced absorption, e = emission. (e) Schematic representation of the two PDI triplet spin-polarization pathways observed in the dyads: SOCT-ISC, leading to selective population of the T_Y sublevel, and RP-ISC, leading to selective population of T_0. The arrows indicate the direction of the transition (red = enhanced absorption, blue = emission).

Singlet oxygen experiments.

So far, our analysis has highlighted the rich spin photophysics of these dyads and demonstrated that the coexistence of two spin-selective mechanisms - SOCT-ISC and RP-ISC - strongly enhances the population of the ^{3*}PDI state, whose quantum yield is typically very low in conventional PDI molecules. Enhanced triplet formation is particularly relevant because triplet states participate in key photochemical processes, including singlet oxygen ($^1O_2$) sensitization, which underpins a wide range of applications spanning photodynamic therapy and photomedicine, photochemistry and green oxidation, and water treatment technologies.[71–75]

To assess the ability of the dyads to promote singlet oxygen generation, we performed $^1O_2$ photoluminescence (PL) measurements by monitoring its characteristic near-infrared emission at ~1270 nm. In the photosensitization process, photoexcitation of the D-A dyads promotes the generation of ^{3*}PDI, which sensitizes molecular oxygen via Dexter-type triplet–triplet energy transfer. Measurements were carried out for the four dyads in toluene solution at room temperature upon photoexcitation at 530 nm; the corresponding spectra are shown in Figure 7. For comparison, the PL intensity was benchmarked against both the PDI molecule and the ZnTPP literature standard. As expected, all samples - except for PDI, which shows no detectable signal due to its very low ISC efficiency - exhibit the characteristic $^1O_2$ emission centered at 1270 nm. [76–78]

The $^1O_2$ emission intensity depends on the bridge length. Dyad **1** reaches approximately two-thirds of the ZnTPP intensity, **1ph** and **2** achieve comparable values, and **3** exhibits a reduced intensity below that of **1**. These trends can be rationalized in

View Article Online
DOI: 10.1039/D6TC01492E

terms of the balance between CT formation and recombination to the low-lying triplet state. Our results indicate that increasing the bridge length from **1** to **1ph** and **2** enhances $^1O_2$ generation, despite transient absorption measurements showing a decrease in the overall CT efficiency. This behavior suggests that CT recombination becomes more effective in populating the PDI triplet state as the donor-acceptor separation increases. When the bridge is further extended, as in **3**, CT formation is significantly suppressed, leading to reduced triplet generation and a corresponding decrease in $^1O_2$ emission, consistent with the experimental observations.

Overall, the $^1O_2$ generation efficiency of our dyads, comparable to that of ZnTPP (Φ = 0.78),[79] demonstrates their excellent sensitization performance. In D-A dyads, $^1O_2$ generation is not governed by the presence of heavy atoms, as in conventional photosensitizers, but rather by the ability of the system to efficiently channel photoexcitation into triplet states. In this context, the use of light-atom organic chromophores that support long-lived triplet states, such as PDI, represents a particularly promising strategy and highlights the strong potential of spin-selective charge-transfer mechanisms for photodynamic therapy applications.

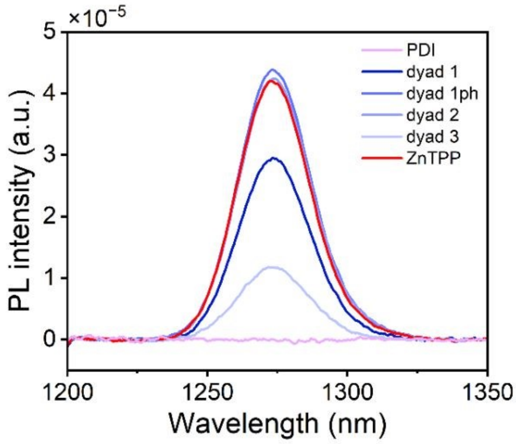

Figure 7. Comparison of the near-infrared photoluminescence (PL) intensity of singlet oxygen sensitized by **dyads 1**, **1ph**, **2**, and **3**, PDI, and ZnTPP (used as a reference standard) in toluene (optical density ≈ 1 for all samples). PDI-based dyads were excited at 530 nm, whereas ZnTPP was excited at 550 nm.

Conclusions

In this study, we report the synthesis, photophysical characterization, and DFT analysis of a new series of donor-acceptor dyads featuring a dithia-aza[4]helicene unit as the electron donor and differing in the length of the ethynylbenzene-containing bridge.

Our multitechnique investigation has enabled a comprehensive rationalization of the mechanisms governing charge transfer and recombination, and of their impact on the spin polarization of the PDI acceptor triplet state, as a function of the ethynylbenzene bridge length. Consistent with previous observations in *p*-phenylene oligomer bridges,[49] we identify a clear crossover from the superexchange to the charge hopping regime, manifested in the non-monotonic dependence of the charge-recombination rate on bridge length.

The resulting spin polarization arises from the subtle interplay between the superexchange magnetic coupling, and the g-values and the hyperfine interactions within the $D^{+\bullet}$ and $A^{-\bullet}$ radical pair. State-of-the-art DFT calculations have enabled us to quantify the extremely weak superexchange couplings in the photoexcited charge-separated states, confirming that the conditions required for the RP-ISC mechanism are met in the compound with the longest bridge. The computational protocol developed here thus provides a predictive framework for the rational design of donor–acceptor dyads with tailored spin properties.

In parallel, we have observed a correlation in the efficiency of singlet oxygen ($^1O_2$) generation, which also exhibits a non-monotonic dependence on bridge length, with the highest efficiency detected for the intermediate bridge length of ***2***. Further investigations will be required to disentangle the underlying contributions and to establish clear design principles for optimizing D/A dyads as singlet-oxygen sensitizers. The high singlet oxygen quantum yields of these donor–acceptor dyads underscore their potential as promising candidates for photodynamic therapy, notably enabling efficient $^1O_2$ generation without incorporating heavy atoms.

Importantly, although all measurements reported here were conducted on racemic mixtures, the new dyads investigated in this study are chiral owing to the presence of the dithia-aza[4]helicene donor unit. Their high racemization barriers allowed efficient separation of the enantiomers by chiral HPLC. This feature opens new opportunities in the field of the chirality-induced spin selectivity (CISS) effect, as opposite enantiomers are expected to display opposite spin selectivity. Such behavior, however, would be observable only in systems where the molecules are unidirectionally aligned (e.g., poled samples). Ongoing work in our group is directed toward this objective.

Data Availability

All data are available via the Zenodo repository or from the corresponding authors upon request.

Acknowledgements

This work has received funding from the European Union's Horizon Europe research and innovation program under the Marie Skłodowska-Curie project PHOTOCODE (proj n. 101104276) and the ERC-Synergy project CASTLE (proj. n. 101071533). Views and opinions expressed are however those of the author(s) only and do not necessarily reflect those of the European Union or the European Commission. Neither the European Union nor the granting authority can be held responsible for them. A.P. and A.C. also acknowledge

View Article Online
DOI: 10.1039/D6TC01492E

funding from the Italian Ministry of University and Research (MUR) under the FIS2 project SPIRO-χ (FIS-2023-01975). Support of Italian MUR through the Dipartimenti di Eccellenza 2023-2027 (DICUS 2.0) and PRIN 2022 project SMART HELIX (2022B3EFJH) is also acknowledged.

Conflicts of interest

There are no conflicts to declare.

References

1 A. Privitera, J. Grüne, A. Karki, W. K. Myers, V. Dyakonov, T. Q. Nguyen, M. K. Riede, R. H. Friend, A. Sperlich and A. J. Gillett, *Adv. Energy Mater.*, 2022, **12**, 2103944..

2 I. Ramirez, A. Privitera, S. Karuthedath, A. Jungbluth, J. Benduhn, A. Sperlich, D. Spoltore, K. Vandewal, F. Laquai and M. Riede, *Nat. Commun.*, 2021, **12**, 471.

3 A. J. Gillett, A. Privitera, R. Dilmurat, A. Karki, D. Qian, A. Pershin, G. Londi, W. K. Myers, J. Lee, J. Yuan, S. J. Ko, M. K. Riede, F. Gao, G. C. Bazan, A. Rao, T. Q. Nguyen, D. Beljonne and R. H. Friend, *Nature*, 2021, **597**, 666–671.

4 J. Grüne, G. Londi, A. J. Gillett, B. Stähly, S. Lulei, M. Kotova, Y. Olivier, V. Dyakonov and A. Sperlich, *Adv. Funct. Mater.*, 2023, **33**, 2212640.

5 A. Rao, A. J. Gillett and R. H. Friend, *Nat. Mater.*, 2022, **21**, 976–978.

6 S. Neumann, O. S. Wenger and C. Kerzig, *Chem. Eur. J.*, 2021, **27**, 4115–4123.

7 G. N. Lim, C. O. Obondi and F. D'Souza, *Angew. Chem. Int. Ed.*, 2016, **55**, 11517–11521.

8 A. Chiesa, A. Privitera, E. Garlatti, G. Allodi, R. Bittl, M. R. Wasielewski, R. Sessoli and S. Carretta, *J. Phys. Chem. Lett.*, 2025, **16**, 5358–5372.

9 A. Privitera, D. Faccio, D. Giuri, E. I. Latawiec, D. Genovese, F. Tassinari, L. Mummolo, M. Chiesa, C. Fontanesi, E. Salvadori, A. Cornia, M. R. Wasielewski, C. Tomasini and R. Sessoli, *Chem. Eur. J.*, 2023, **29**, e202301005.

10 A. Chiesa, A. Privitera, E. Macaluso, M. Mannini, R. Bittl, R. Naaman, M. R. Wasielewski, R. Sessoli and S. Carretta, *Adv. Mater.*, 2023, 35, 2300472.

11 G. C. Mantel, K. T. Kairys, M. L. Williams, M. D. Krzyaniak, R. M. Young, R. Tempelaar and M. R. Wasielewski, *J. Am. Chem. Soc.*, 2025, **147**, 29592-29601..

12 H. J. Eckvahl, G. Copley, R. M. Young, M. D. Krzyaniak and M. R. Wasielewski, *J. Am. Chem. Soc.*, 2024, **146**, 24125–24132.

13 H. J. Eckvahl, N. A. Tcyrulnikov, A. Chiesa, J. M. Bradley, R. M. Young, S. Carretta, M. D. Krzyaniak and M. R. Wasielewski, *Science*, 2023, **382**, 197-201.

14 Y. Shen and C. F. Chen, *Chem. Rev.*, 2012, **112**, 1463-1535.

15 S. Hiroto and M. Chujo, *Chem. Asian J.*, 2025, **20**, e202400830.

16 R. Henry Martin, *Angew. Chem. Int. Ed.*, 1974, **13**, 649–660.

17 M. Lupi, O. Salmi, C. Viglianisi and S. Menichetti, *Adv. Synth. Catal.*, 2023, **365**, 1705–1712.

18 S. Menichetti, S. Cecchi, P. Procacci, M. Innocenti, L. Becucci, L. Franco and C. Viglianisi, *Chem. Commun.*, 2015, **51**, 11452–11454.

19 R. Amorati, L. Valgimigli, A. Baschieri, Y. Guo, F. Mollica, S. Menichetti, M. Lupi and C. Viglianisi, *ChemPhysChem*, 2021, **22**, 1446–1454.

20 G. Lamanna, C. Faggi, F. Gasparrini, A. Ciogli, C. Villani, P. J. Stephens, F. J. Devlin and S. Menichetti, *Chem. Eur. J.*, 2008, **14**, 5747–5750.

21 M. Fusè, M. Lupi, E. Machalska, G. Mazzeo, S. Abbate, J. Bloino, C. Viglianisi, S. Menichetti and G. Longhi, *Chem. Asian J.*, 2025, **20**, e202401752..

22 S. Menichetti, C. Faggi, M. Onori, S. Piantini, M. Ferreira, S. Rocchi, M. Lupi, I. Marin, M. Maggini and C. Viglianisi, *Eur. J. Org. Chem.*, 2019, **2019**, 168–175.

23 V. Kiran, S. P. Mathew, S. R. Cohen, I. Hernández Delgado, J. Lacour and R. Naaman, *Adv. Mater.*, 2016, **28**, 1957–1962.

24 J. Crassous, M. J. Fuchter, D. E. Freedman, N. A. Kotov, J. Moon, M. C. Beard and S. Feldmann, *Nat. Rev. Mater.*, 2023, **8**, 365-371.

25 R. Rodríguez, C. Naranjo, A. Kumar, K. Dhbaibi, P. Matozzo, F. Camerel, N. Vanthuyne, R. Gómez, R. Naaman, L. Sánchez and J. Crassous, *Chem. Eur. J.*, 2023, **29**, e202302254.

26 S. Cadeddu, R. Chowdhury, C. Delpiano Cordeiro, S. Parmar, A. Kramer, M. Cordier, A. Pensel, N. Vanthuyne, R. Sessoli, M. Chiesa, Y. K. Liao, R. H. Friend, E. Salvadori, J. Autschbach and J. Crassous, *J. Am. Chem. Soc.*, 2025, **147**, 23643–23653.

View Article Online
DOI: 10.1039/D6TC01402E

27 N. Giaconi, M. Lupi, T. K. Das, A. Kumar, L. Poggini, C. Viglianisi, L. Sorace, S. Menichetti, R. Naaman, R. Sessoli and M. Mannini, *J. Mater. Chem. C Mater.*, 2024, **12**, 10029–10035.

28 N. Giaconi, L. Poggini, M. Lupi, M. Briganti, A. Kumar, T. K. Das, A. L. Sorrentino, C. Viglianisi, S. Menichetti, R. Naaman, R. Sessoli and M. Mannini, *ACS Nano*, 2023, **17**, 15189–15198.

29 N. Giaconi, A. L. Sorrentino, L. Poggini, M. Lupi, V. Polewczyk, G. Vinai, P. Torelli, A. Magnani, R. Sessoli, S. Menichetti, L. Sorace, C. Viglianisi and M. Mannini, *Angew. Chem. Int. Ed.*, 2021, **60**, 15276–15280.

30 M. R. Wasielewski, *Chem. Rev.*, 1992, **92**, 435-461.

31 S. M. Harvey and M. R. Wasielewski, *J. Am. Chem. Soc.*, 2021, **143**, 15508-15529.

32 W. B. Davis, M. A. Ratner and M. R. Wasielewski, *J. Am. Chem. Soc.*, 2001, **123**, 7877–7886.

33 A. B. Ricks, G. C. Solomon, M. T. Colvin, A. M. Scott, K. Chen, M. A. Ratner and M. R. Wasielewski, *J. Am. Chem. Soc.*, 2010, **132**, 15427–15434.

34 M. N. Paddon-Row, *Acc. Chem. Rev.*, 1994, **27**, 18-25.

35 D. M. Guldi, M. Maggini, G. Scorrano and M. Prato, *J. Am. Chem. Soc.*, 1997, **119**, 974-980.

36 G. Agnoloni, A. Chiesa, R. M. Young, F. Totti, S. Menichetti, C. Viglianisi, M. R. Wasielewski, S. Carretta, A. Privitera and R. Sessoli, *J. Am. Chem. Soc.*, 2026, **148**, Accepted.

37 D. M. Cadena, J. K. Sowa, D. E. Cotton, C. D. Wight, C. L. Hoffman, H. R. Wagner, J. T. Boette, E. K. Raulerson, B. L. Iverson, P. J. Rossky and S. T. Roberts, *J. Am. Chem. Soc.*, 2022, **144**, 22676-22688.

38 T. Yanai, D. P. Tew and N. C. Handy, *Chem. Phys. Lett.*, 2004, **393**, 51–57.

39 Y. Shao, M. Head-Gordon and A. I. Krylov, *J. Chem. Phys.*, 2003, **118**, 4807–4818.

40 E. Selenius, A. E. Sigurdarson, Y. L. A. Schmerwitz and G. Levi, *J. Chem. Theory Comput.*, 2024, **20**, 3809–3822.

41 F. Neese, *Wiley Interdiscip. Rev. Comput. Mol. Sci.*, 2012, **2**, 73–78.

42 R. M. Young, S. M. Dyar, J. C. Barnes, M. Juríček, J. F. Stoddart, D. T. Co and M. R. Wasielewski, *J. Phys. Chem. A*, 2013, **117**, 12438–12448.

43 P. E. Hartnett, E. A. Margulies, H. S. S. R. Matte, M. C. Hersam, T. J. Marks and M. R. Wasielewski, *Chem. Mater.*, 2016, **28**, 3928–3936.

44 A. F. Coleman, M. Chen, J. Zhou, J. Y. Shin, Y. Wu, R. M. Young and M. R. Wasielewski, *J. Phys. Chem. C*, 2020, **124**, 10408–10419.

45 T. Mori and Y. Inoue, *Angew. Chem. Int. Ed.*, 2005, **117**, 2638–2641.

46 K. Chen, I. V. Kurganskii, X. Zhang, A. Elmali, J. Zhao, A. Karatay and M. V. Fedin, *Chem. Eur. J.*, 2021, **27**, 7572–7587.

47 N. Rehmat, A. Toffoletti, Z. Mahmood, X. Zhang, J. Zhao and A. Barbon, *J. Mater. Chem. C.*, 2020, **8**, 4701–4712.

48 W. E. Ford and P. V Kamat, *J. Phys. Chem.*, 1987, **91**, 6373-6380.

49 E. A. Weiss, M. J. Ahrens, L. E. Sinks, A. V. Gusev, M. A. Ratner and M. R. Wasielewski, *J. Am. Chem. Soc.*, 2004, **126**, 5577–5584.

50 E. A. Weiss, M. J. Tauber, R. F. Kelley, M. J. Ahrens, M. A. Ratner and M. R. Wasielewski, *J. Am. Chem. Soc.*, 2005, **127**, 11842–11850.

51 E. I. Latawiec, A. Chiesa, Y. Qiu, N. A. Tcyrulnikov, R. M. Young, S. Carretta, M. D. Krzyaniak and M. R. Wasielewski, *Proc. Natl. Acad. Sci. U. S. A.*, 2025, **122**, e2515120122.

52 J. M. Alzola, N. E. Powers-Riggs, N. T. La Porte, R. M. Young, T. J. Marks and M. R. Wasielewski, *J. Porphyr. Phthalocyanines*, 2020, **24**, 143–152.

53 B. Zhang, H. Soleimaninejad, D. J. Jones, J. M. White, K. P. Ghiggino, T. A. Smith and W. W. H. Wong, *Chem. Mater.*, 2017, **29**, 8395–8403.

54 Z. E. X. Dance, Q. Mi, D. W. McCamant, M. J. Ahrens, M. A. Ratner and M. R. Wasielewski, *J. Phys. Chem. B*, 2006, **110**, 25163–25173.

55 R. Carmieli, T. A. Zeidan, R. F. Kelley, Q. Mi, F. D. Lewis and M. R. Wasielewski, *J. Phys. Chem. A*, 2009, **113**, 4691–4700.

56 N. Rehmat, I. V. Kurganskii, Z. Mahmood, Q. L. Guan, J. Zhao, Y. H. Xing, G. G. Gurzadyan and M. V. Fedin, *Chem. Eur. J.*, 2021, **27**, 5521–5535.

57 A. Mambetov, A. Sukhanov, X. Zhang, J. Zhao and V. Voronkova, *Appl. Magn. Reson.*, 2024, **55**, 1553–1567.

58 T. Miura, R. Carmieli and M. R. Wasielewski, *J. Phys. Chem. A*, 2010, **114**, 5769–5778.

View Article Online
DOI: 10.1039/D6TC01492E

59 H. Weissman, E. Shirman, T. Ben-Moshe, R. Cohen, G. Leitus, L. J. W. Shimon and B. Rybtchinski, *Inorg. Chem.*, 2007, **46**, 4790–4792.

60 T. Okada, I. Karakl, E. Matsuzawa, N. Malaga, Y. Sakata and S. Mlsuml, *J. Phys. Chem.*, 1981, **85**, 3957-3960.

61 M. R. Wasielewski, D. G. Johnson, W. A. Svec, K. M. Kersey and D. W. Minsek, *J. Am. Chem. Soc.*, 1988, **110**, 7219-7221.

62 H. Van Willigen, G. Jones and M. S. Farahat, *J. Phys. Chem.*, 1996, **100**, 3312-3316.

63 I. R. Gould, J. A. Boiani, E. B. Gaillard, J. L. Goodman and S. Farid, *J. Phys. Chem. A*, 2003, **107**, 3515–3524.

64 M. Hussain, A. M. El-Zohry, Y. Hou, A. Toffoletti, J. Zhao, A. Barbon and O. F. Mohammed, *J. Phys. Chem. B*, 2021, **125**, 10813–10831.

65 Y. Zhao, R. Duan, J. Zhao and C. Li, *Chem. Commun.*, 2018, **54**, 12329–12332.

66 Z. Wang, L. Ma, H. Zhao, Y. Wan, X. F. Zhang, Y. Li, Z. Kuang and A. Xia, *Phys. Chem. Chem. Phys.*, 2023, **25**, 24386–24394.

67 Z. Wang, M. Ivanov, Y. Gao, L. Bussotti, P. Foggi, H. Zhang, N. Russo, B. Dick, J. Zhao, M. Di Donato, G. Mazzone, L. Luo and M. Fedin, *Chem. Eur. J.*, 2020, **26**, 1091–1102.

68 J. T. Buck, A. M. Boudreau, A. DeCarmine, R. W. Wilson, J. Hampsey and T. Mani, *Chem*, 2019, **5**, 138–155.

69 D. Ranieri, A. Privitera, F. Santanni, K. Urbanska, G. J. Strachan, B. Twamley, E. Salvadori, Y. K. Liao, M. Chiesa, M. O. Senge, F. Totti, L. Sorace and R. Sessoli, *Angew. Chem. Int. Ed.*, 2023, **62**, e202312936.

70 D. Ranieri, F. Santanni, A. Privitera, A. Albino, E. Salvadori, M. Chiesa, F. Totti, L. Sorace and R. Sessoli, *Chem. Sci.*, 2022, **14**, 61–69.

71 L. N. Zhang, Y. F. Wei, X. Y. Ran, L. Shi, Z. Y. Wang, S. Y. Chen, C. Yi, X. Q. Yu and K. Li, *JACS Au*, 2025, **5**, 3982–3993.

72 A. Gorman, J. Killoran, C. O'Shea, T. Kenna, W. M. Gallagher and D. F. O'Shea, *J. Am. Chem. Soc.*, 2004, **126**, 10619–10631.

73 J. Deckers, T. Cardeynaels, L. Lutsen, B. Champagne and W. Maes, *ChemPhysChem*, 2021, **22**, 1488–1496.

74 F. Wilkinson, W. P. Helman and A. B. Ross, *J. Phys. Chem. Ref. Data*, 1993, **22**, 113–262.

75 Z. Xiao and D. Dolphin, *Tetrahedron*, 2002, **58**, 9111-9116.

76 D. R. Kearns, *Chem. Rev.*, 1971, **71**, 4, 395-427.

77 R. Schmidt, *Photochem. Photobiol.*, 2007, **82**, 1161–1177.

78 S. Jockusch, N. J. Turro, E. K. Thompson, M. Gouterman, J. B. Callis and G. E. Khalil, *Photochem. Photobiol. Sci.*, 2008, **7**, 235–239.

79 F. Nifiatis, J. C. Athas, K. Don, D. Gunaratne, Y. Gurung, K. M. Monette and P. J. Shivokevich, *Open Spectrosc. J.*, 2011, **5**, 1-12.

View Article Online
DOI: 10.1039/D6TC01492E

All data reported in this manuscript will be made available through the open-access Zenodo repository of the ERC Synergy Project CASTLE (https://zenodo.org/communities/castle-ercsynergy-101071533/) and from the corresponding authors upon request.